Supplement of Atmos. Chem. Phys., 22, 15489–15508, 2022
https://doi.org/10.5194/acp-22-15489-2022-supplement

Supplement of

How do Cl concentrations matter for the simulation of CH_4 and $\delta^{13}C(CH_4)$ and estimation of the CH_4 budget through atmospheric inversions?

Joël Thanwerdas et al.

Correspondence to: Joël Thanwerdas (joel.thanwerdas@lsce.ipsl.fr)

The Supplementary Material provides additional information regarding the three methods adopted to estimate the CH_4 fluxes and isotopic source signature adjustments obtained with top-down approaches (Sect. S1, Sect. S2 and Sect. S3). Additional information regarding the multiple sensitivity simulations (Sect. S1, Figure S1, Figure S2, Figure S3, Table S1 and Table S2) are also provided. Also, a demonstration of the formula given in Sect. 3.2 in the main manuscript is provided (Sect. S4). Tables S5 and S6 provide a list of CH_4 and $\delta^{13}C(CH_4)$ surface stations used in this study. Table S3 and Figure S4 provide the locations and a list of CH_4 AirCore profiles. Table S4 and Figure S5 provide the locations and a list of $\delta^{13}C(CH_4)$ balloons profiles. Figure S6 provides maps of seasonal cycle amplitudes for multiple configurations. Figure S7 provides the time-series of the biases in atmospheric CH_4 mass.

S 1 Method 1 – 3-D variational inversion

This section describes the Method 1 (M1) used in the main manuscript. It is based on the 3-D variational inversion system designed by Thanwerdas et al. (2022). Configurations adopted for running inversions with this system is presented below.

S 1.1 The chemistry-transport model

The chemistry-transport model (CTM) LMDz-SACS is presented in the main manuscript. Oxidations by OH, $O(^1D)$ and Cl were included in the chemical scheme of LMDz-SACS. Time-varying 3-D fields with daily resolution were prescribed offline for each oxidant species to simulate the associated chemical loss. These fields were simulated by the LMDz-INCA chemistry model (Hauglustaine et al., 2004) with the same meteorology as in the simulations of this study.

The resulting OH field, named OH-INCA, exhibits a global mass-weighted tropospheric concentration of 11.1×10^5 molec. cm^{-3} over the 1998-2018 period, consistent with the previous estimates from Zhao et al. (2019) (11.7×10^5 molec. cm^{-3}), estimates from Prather et al. (2012) ($11.2 \pm 1.3 \times 10^5$ molec. cm^{-3}), and well within the range derived from the Atmospheric Chemistry and climate Model Intercomparison Project (ACCMIP) (10.3-13.4 $\times 10^5$ molec. cm^{-3} ; Voulgarakis et al., 2013). The inter-hemispheric ratio is 1.14, lower than the mean value of 1.3 inferred by Zhao et al. (2019) but more consistent with an inter-hemispheric parity suggested by Patra et al. (2014). OH-INCA globally-averaged concentrations increase by 4 % between 2002 and 2014.

S 1.2 Inverse modelling with a variational approach

Inversions are powerful methods that optimize our prior knowledge of a state (here emissions) by assimilating data (here atmospheric CH_4 mole fractions and isotopic composition). Inversions were performed using the Community Inversion Framework (CIF) (Berchet et al., 2021). This framework was designed to rationalize and bridge development efforts made by the scientific community within the same flexible, transparent and open-source system. This system was recently enhanced by Thanwerdas et al. (2022) to assimilate $\delta^{13}\mathrm{C(CH_4)}$ together with CH_4 observations and optimize source signatures $\delta^{13}\mathrm{C(CH_4)}_{\mathrm{source}}$ together with CH_4 emissions.

The notations introduced here to describe the variational inversion method follow the convention defined by Ide et al. (1997) and Rayner et al. (2019). $\mathbf{x}$ is the control vector and includes all the variables optimized by the inversion system. Prior information about the control variables is included in the vector $\mathbf{x}^{\mathrm{b}}$. Its associated errors are assumed to be unbiased and Gaussian, and are described within the error covariance matrix $\mathbf{B}$.

The observation vector $\mathbf{y}^{\mathrm{o}}$ includes here all available observations, namely atmospheric CH_4 and $\delta^{13}\mathrm{C(CH_4)}$ data, over the full simulation time-window. The associated errors are also assumed to be unbiased and Gaussian, and are described within the error covariance matrix $\mathbf{R}$. This matrix accounts for all errors contributing to mismatches between simulated and observed values.

$\mathscr{H}$ is the observation operator that projects the control vector $\mathbf{x}$ into the observation space. This operator mainly consists of the CTM but is also followed by spatial, time and isotope-conversion operators, which interpolate the simulated fields to produce simulated equivalents of the observed mole fractions and isotopic composition at specific locations and times, making the simulations and observations comparable.

In a variational formulation of the inversion problem that allows for $\mathscr{H}$ non-linearity, the cost function J is defined as :

$$J(\mathbf{x}) = \frac{1}{2}(\mathbf{x}-\mathbf{x}^{\mathrm{b}})^{\mathrm{T}}\mathbf{B}^{-1}(\mathbf{x}-\mathbf{x}^{\mathrm{b}}) + \frac{1}{2}(\mathscr{H}(\mathbf{x})-\mathbf{y}^{\mathrm{o}})^{T}\mathbf{R}^{-1}(\mathscr{H}(\mathbf{x})-\mathbf{y}^{\mathrm{o}}) \tag{S.1}$$

Here, the minimum of J is reached iteratively with the descent algorithm M1QN3 (Gilbert and Lemaréchal, 1989) that requires several computations (40-50) of the gradient of J with respect to the control vector $\mathbf{x}$:

$$\nabla J_{\mathbf{x}} = \mathbf{B}^{-1}(\mathbf{x}-\mathbf{x}^{\mathrm{b}}) + \mathscr{H}^{*}(\mathbf{R}^{-1}(\mathscr{H}(\mathbf{x})-\mathbf{y}^{\mathrm{o}})) \tag{S.2}$$

$\mathscr{H}^{*}$ denotes the adjoint operator of $\mathscr{H}$.

All inversions performed as part of this study shared the same configuration. The only difference is the prescribed Cl sink. All inversions assimilated CH_4 and $\delta^{13}\mathrm{C(CH_4)}$ observations over the 1998-2018 period. CH_4 emissions and $\delta^{13}\mathrm{C(CH_4)}$ source signatures for five categories of emissions were optimized : biofuels-biomass burning (BB), wetlands (WET), fossil fuels and geological sources (FFG), agriculture and waste (AGW) and other natural sources (NAT). CH_4 and $\delta^{13}\mathrm{C(CH_4)}$ initial conditions were also optimized (see Sect. S 1.6 of the present document).

S 1.3 Prior emissions and signatures

For prior CH_4 emissions, we adopted the bottom-up estimates compiled for the inversions performed as part of the Global Methane Budget (Saunois et al., 2020). Anthropogenic (including biofuels) and fire emissions are based on the EDGARv4.3.2 database (Janssens-Maenhout et al., 2019) and the GFED4s databases (van der Werf et al., 2017), respectively. Statistics from British Petroleum (BP) and the Food and Agriculture Organization of the United Nations (FAO) have been used to extend the EDGARv4.3.2 database, ending 2012, until 2017. The natural sources emissions are based on averaged literature values : Poulter et al. (2017) for wetlands, Kirschke et al. (2013) for termites, Lambert and Schmidt (1993), Etiope (2015) for geological (onshore) sources and oceanic sources that include geological (offshore) and hydrates sources. Prior emissions for 2018 are set equal to 2017. Globally averaged emissions over the 1998-2018 period are listed in Table S1.

BB emissions are the combination of biomass burning emissions from GFED4s and biofuels burning emissions from EDGARv4.3.2. FFG emissions are the combination of oil, gas, coal and industry emissions from EDGARv4.3.2 and geological (onshore) sources from Etiope (2015) which have been scaled down to 15.0 $\text{TgCH}_4\,\text{yr}^{-1}$ in the protocol of Saunois et al. (2020). AGW emissions are the combination of enteric fermentation, rice agriculture, manure management and waste emissions from EDGARv4.3.2. NAT emissions are the combination of termites and oceanic emissions, i.e., natural emissions apart from wetlands and geological sources.

Emissions are optimized at the grid cell scale (one scaling factor per grid cell). For each category, diagonal elements of the matrix **B** are filled with the variances set to 100 % of the square of the maximum of prior emissions over the cell and its eight neighbours during each month. Spatial error correlations (off-diagonal elements) are prescribed using an e-folding correlation length of 500 km on land and 1000 km over the oceans, without any correlation between land and ocean grid points. No temporal error correlations are prescribed.

$\delta^{13}\text{C(CH}_4)_{\text{source}}$ isotopic source signatures for each emissions category are also optimized and therefore included in the control vector. Prior information is built using the references given in Table S2. When regional information could be found, regional source signature values were prescribed onto 11 continental regions (see Fig. S2, lower-right panel). We optimized source signatures at the regional scale rather than at the grid cell scale (i.e., using only one scaling factor per region), as optimizing at the grid cell scale could result in substantial posterior differences between two adjacent grid cells. At present, there is not enough data to corroborate, explain or reject such differences.

Livestock source signatures have been likely decreasing over time since the 1990s due to changes in C3/C4 diet within the major livestock producing countries (Chang et al., 2019). Also, FFG regional source signatures can vary over time due to variations in the contributions from different sectors (coal, oil and gas) to the emissions of a specific region (Schwietzke et al., 2016; Feinberg et al., 2018). For AGW and FFG source signatures, we therefore optimize one scaling factor per year, for each region. As for the other emission categories, only one scaling factor for the entire period and for each region is optimized. Error correlations are prescribed by following the same methods as that for CH_4 emissions.

S 1.4 Uncertainties in source signatures

$\delta^{13}\text{C(CH}_4)_{\text{source}}$ uncertainty values that are used to fill the diagonal elements of the matrix **B** are summarized in Table S1. These values have been chosen by compiling data from several studies (Sherwood et al., 2017; Ganesan et al., 2018; Feinberg et al., 2018; Zazzeri et al., 2016). As the inversion system is used over a long time period for the first time, a global uncertainty value has been prescribed for all emission categories. For BB sources, Sherwood et al. (2017) indicates a standard deviation of about 20 %. However, this value is not weighted by proportion C3 versus C4 vegetation. Therefore, we decided to inflate this uncertainty up to 30 %.

S 1.5 Observations

Measurements retrieved by the NOAA-ESRL Global Monitoring Laboratory (NOAA GML) network and analyzed by the Institute of Artic and Alpine Research (INSTAAR) are assimilated. 79 stations (among which 4 mobile stations) provided CH_4 measurements between 1998 and 2018 (not necessarily over the full period), 22 stations provided $\delta^{13}C(CH_4)$ measurements between 1998 and 2018 (see Fig. S3).

Missing CH_4 measurement errors were filled with the maximum value at the station over the monitoring period. As for $\delta^{13}C(CH_4)$ measurements, missing errors were filled with a value of 0.1 ‰ and 3 ‰, respectively (Quay et al., 1999). We also removed outliers outside three times the residual standard deviations as such extreme values cannot be reasonably captured at the resolution of LMDz. Variances (diagonal elements) in the covariance matrix **R** were defined as the sum of the measurement and model errors.

For each station and each year, we used the Residual Standard Deviation (RSD) between the measurements and a fitting curve function as a proxy for the model error (Locatelli et al., 2015, 2013; Cressot et al., 2014; Yver et al., 2011; Bousquet et al., 2006; Rodenbeck et al., 2003). The fitting function includes 3 polynomial parameters (quadratic) and 8 harmonic parameters, sinus and cosinus, as in Masarie and Tans (1995).

More information about the surface stations is provided in Tables S5 and S6 as well as in Figure S3.

S 1.6 Initial conditions

To infer initial conditions in 1998 for CH_4 and $\delta^{13}C(CH_4)$, we run a shorter inversion between 1988 and 1998 using the configuration described in the previous sections. The state of the atmosphere in January 1998 was used as initial conditions for the 1998-2018 inversions.

We assimilated CH_4 measurements from the NOAA GML network (56 stations) and $\delta^{13}C(CH_4)$ measurements retrieved at 5 stations across the globe by the University of Washington (UW) between 1988 and 1996 (Quay et al., 1999; Bousquet et al., 2006) that we offset by 0.1 ‰ to account for measurement offsets between INSTAAR and UW (Umezawa et al., 2018).

As we acknowledge that this method is not perfect considering the equilibration time of the isotopic composition (Tans, 1997), we also prescribe large uncertainties in these initial conditions : 10 % for CH_4 and 3 % for $\delta^{13}C(CH_4)$.

S 2 Method 2 − 1-D analytical inversion

This section describes the Method 2 (M2) used in the main manuscript. For the purpose of this study, we built an analytical inversion framework based on a very simple one-box model representing the atmosphere. We use the same notations introduced in Sect. S 1.2.

S 2.1 The control vector

The control vector **x** includes monthly global CH_4 fluxes and monthly global isotopic source signature $\delta^{13}C(CH_4)_{source}$ for the 1998-2018 period, i.e. $252 \times 2 = 504$ values. We also include two increments for CH_4 and $\delta^{13}C(CH_4)$ initial conditions. The prior global fluxes and source signatures are the same as in Sect. S1.

To fill the diagonal of the matrix **B**, we prescribe a flux uncertainty of 50 $TgCH_4\ yr^{-1}$ (one standard deviation) and a source isotopic signature uncertainty of 5 ‰. As for initial conditions, we prescribe an uncertainty of 5 ppb for CH_4 and 0.1 ‰ for $\delta^{13}C(CH_4)$.

S 2.2 The observation vector

The $\delta^{13}C(CH_4)$ data presented in Sect. S1 is also used for the inversions performed with this inversion framework. However, the observations are globally averaged using a similar method to Masarie and Tans (1995) to preserve only a global monthly time-series that can be assimilated in our inversion. As for CH_4, we use the monthly data available at https://gml.noaa.gov/ccgg/trends_ch4/. We prescribe an observational uncertainty of 2 ppb for CH_4 and 0.1 ‰ for $\delta^{13}C(CH_4)$.

S 2.3 The observation operator

The observation operator $\mathscr{H}$ (one-box model) consists in two mass-conservation equations for $^{12}CH_4$ et $^{13}CH_4$:

$$\begin{cases} \frac{dB_{12}}{dt} = S_{12} - \frac{B_{12}}{\tau_{12}} \\ \frac{dB_{13}}{dt} = S_{13} - \frac{B_{13}}{\tau_{13}} \end{cases} \tag{S.3}$$

B_{12} et B_{13} are the total masses of $^{12}CH_4$ and $^{13}CH_4$ in the atmosphere, respectively. τ_{12} and τ_{13} are the chemical lifetimes of $^{12}CH_4$ and $^{13}CH_4$ in the atmosphere, respectively. Their numerical values are based on the outputs of the forward simulations performed for each scenario (FWD-*) and are calculated by dividing the tracer total mass in the atmosphere by the total sink. S_{12} and S_{13} are the global mass fluxes of $^{12}CH_4$ and $^{13}CH_4$, respectively. They are calculated using the total CH_4 fluxes and source signatures included in the control vector :

$$\begin{cases} F_{12} = \frac{M_{12}}{M_T} \cdot \frac{1}{1+A} \cdot F_T \\ F_{13} = \frac{M_{13}}{M_T} \cdot \frac{A}{1+A} \cdot F_T \end{cases} \tag{S.4}$$

with

$$A = (1+\delta^{13}\mathrm{C}(\mathrm{CH4})_{\mathrm{source}})\cdot R_{\mathrm{std}} \tag{S.5}$$

F_T, F_{12} and F_{13} are the $\mathrm{CH_4}$, $^{12}\mathrm{CH_4}$ and $^{13}\mathrm{CH_4}$ mass fluxes, respectively. M_T, M_{12} and M_{13} are the $\mathrm{CH_4}$, $^{12}\mathrm{CH_4}$ and $^{13}\mathrm{CH_4}$ molar masses, respectively. After the simulation, we retrieve the total mass of $\mathrm{CH_4}$, denoted by B, and the atmospheric isotopic composition $\delta^{13}\mathrm{C}(\mathrm{CH_4})$:

$$\begin{cases} B = (\dfrac{B_{12}}{M_{12}} + \dfrac{B_{13}}{M_{13}})\cdot M_T \\ \delta^{13}\mathrm{C}(\mathrm{CH_4}) = \dfrac{\frac{B_{13}}{B_{12}}\cdot\frac{M_{12}}{M_{13}}}{R_{\mathrm{std}}} - 1 \end{cases} \tag{S.6}$$

To compare the total atmospheric $\mathrm{CH_4}$ mass and the observed $\mathrm{CH_4}$ mole fraction at the surface, we use a conversion factor in $\mathrm{TgCH_4^{-1}}$ ppb that is calculated using the outputs of the forward simulations (FWD-*) by dividing the tracer total mass by the tropospheric mass-weighted average of mole fractions. Also, throughout the study, quantities in molec. $\mathrm{cm^{-3}}$ are averaged using a volume-weighted averaging and quantities in volume mixing ratio are averaged using a mass-weighted average.

S 2.4 The analytical solution

If the observation operator is assumed to be linear, the solution of this inversion problem is :

$$\mathbf{x}^{\mathrm{a}} = \mathbf{x}^{\mathrm{b}} + \mathbf{B}\mathbf{H}^{\mathrm{T}}(\mathbf{R}+\mathbf{H}\mathbf{B}\mathbf{H}^{\mathrm{T}})^{-1}(\mathbf{y}^{\mathrm{o}} - \mathbf{H}\mathbf{x}^{\mathrm{b}}) \tag{S.7}$$

Here, we cannot consider that the observation operator is linear due to the isotopic operations and the chemistry reactions (accounting for in the lifetime). If the problem is assumed to be only slightly non-linear, an iterative inversion procedure can be used in which the system is linearized around the current control vector $\mathbf{x}^{\mathrm{a}}_i$ at each iteration i. Under these conditions, the expression of the optimal control vector becomes, for iteration $i+1$ using a formulation at fixed point $\mathbf{x}^{\mathrm{b}}$ (Tarantola, 1987) :

$$\mathbf{x}^{\mathrm{a}}_{i+1} = \mathbf{x}^{\mathrm{b}} + \mathbf{B}\mathbf{H}^{\mathrm{T}}_{\mathbf{x}^{\mathrm{a}}_i}(\mathbf{R}+\mathbf{H}_{\mathbf{x}^{\mathrm{a}}_i}\mathbf{B}\mathbf{H}^{\mathrm{T}}_{\mathbf{x}^{\mathrm{a}}_i})^{-1}(\mathbf{y}^{\mathrm{o}} - \mathscr{H}(\mathbf{x}^{\mathrm{a}}_i) + \mathbf{H}_{\mathbf{x}^{\mathrm{a}}_i}(\mathbf{x}^{\mathrm{a}}_i - \mathbf{x}^{\mathrm{b}})) \tag{S.8}$$

This formulation requires to derive the tangent-linear operations of the forward model and to calculate the tangent-linear operator around the current control vector $\mathbf{x}^{\mathrm{a}}_i$ at each iteration. The convergence is reached after only three iterations.

S 3 Method 3 – Simple estimation based on forward simulations

The method 3 does not require to run inversions. It is based on the outputs of forward simulations (FWD-*) performed with different prescribed Cl field. We demonstrate here that we can easily infer the adjustment value/increment that an inversion system would apply to the prior global flux and the globally-averaged isotopic source signature in order to fit the observational data.

In a one-box model, the temporal evolution of the CH_4 total mass is described by the equation below :

$$\frac{dB}{dt} = S - \frac{B}{\tau} \tag{S.9}$$

where B is the mass of CH_4 in the atmosphere in $TgCH_4$, S is the source in $TgCH_4\,yr^{-1}$ and τ is the chemical lifetime of CH_4 in the atmosphere in yr. If the total mass of CH_4 is increasing in response to a flux enhancement, the total sink will also increase and lead to a stabilization of the total mass after several decades.

In this study, the bias between the CH_4 atmospheric masses is caused by a change in τ because we modify the Cl field. The evolution of the bias b can therefore be described by the equation :

$$\frac{db}{dt} = \frac{d(B_2 - B_1)}{dt} = -\frac{B_1}{\tau_1} + \frac{B_2}{\tau_2} \tag{S.10}$$

Fig S7 shows that, after 21 years of simulation, this bias appears to be tending towards a stabilized value.

In a surface-based inversion (i.e., an inversion assimilating observations from surface stations) without sink optimization, the bias is compensated for by a correction of the CH_4 global surface flux $S + \Delta S$. The inversion system therefore provides an answer to the question : "What is the value of ΔS that will offset the bias caused by a change in the prescribed sink ?". The temporal evolution of the bias between a simulation and the reference simulation can therefore be described by the equation :

$$\frac{db}{dt} = \Delta S - \frac{b}{\tau_{ref}} \tag{S.11}$$

τ_{ref} denotes the chemical lifetime in the reference simulation, namely the lifetime in INV-Wang / FWD-Wang. We assume that ΔS is constant over time because the contribution from the Cl sink to the atmospheric lifetime of CH_4 is very small and also because the inter-annual variability of the Cl sink is below 4 % of the mean value for all Cl fields. M1 and M2 results confirm that the inter-annual variations of adjustments (see error bars in Fig. 3 in the main manuscript) are below 10 % of the mean value. Furthermore, we assume τ_{ref} to be constant over time because the variation around the mean value is below 2 %.

Under these assumptions, the solution of this equation is :

$$b(t) = \Delta S \times \tau_{ref} \times (1 - e^{-\frac{t}{\tau_{ref}}}) \tag{S.12}$$

The value of ΔS can be obtained by analyzing the temporal evolution of the bias and, in particular, by looking at the value of the bias when it is stabilized. Here, after 21 years of simulation, the stabilization is not reached yet. Therefore, we extend our results by applying a curve fitting function to our simulated values :

$$b_X(t) = A_X \times \tau_{ref} \times (1 - e^{-\frac{t}{\tau_{ref}}}) \tag{S.13}$$

A_X is a constant that the curve fitting algorithm returns in order to maximize the agreement between the simulated values and the curve fitting function. Using this function, the results are extended until 2070 to reach a clear stabilization of the simulated biases.

An estimate of ΔS is provided by the coefficient A_X. This theoretical framework is valid for both $^{12}CH_4$ and $^{13}CH_4$ isotopologues. Therefore, we use it for both tracers and to derive numerical values for both ΔS_{12} and ΔS_{13}. With these values, it is easy to find ΔS and $\Delta\delta^{13}C(CH_4)_{\text{source}}$.

S 4 Calculating the stabilization value of the globally-averaged isotopic source signature

Here, we demonstrate the result used in Sect. 3.2 of the main paper. That is, the $\delta^{13}C(CH_4)$ bias, denoted by $\Delta\delta_a$, between two simulations prescribing the same CH_4 source, the same source signature δ_s but different isotopic fractionations ε, tends to a steady-state value (steady-state) that is given by the formula below:

$$\Delta\delta_a \approx -\Delta\varepsilon \cdot (1+\delta_s) \tag{S.14}$$

For ease of demonstration, this relationship is shown by approximating that the tropospheric mixing ratios of $^{12}CH_4$ are equal to those of CH_4 and we simplify the problem by reducing it to a one-box model problem.

If we start from a mass-conservation equation in a one-box problem, we have :

$$\begin{cases} \dfrac{dB}{dt} = S - k \cdot B \\ \dfrac{dB_{13}}{dt} = S_{13} - k_{13} \cdot B_{13} \end{cases} \tag{S.15}$$

where B et B_{13} are the total masses of $^{12}CH_4$ et $^{13}CH_4$ in the atmosphere, respectively. k and k_{13} are the reaction rate constants of $^{12}CH_4$ and $^{13}CH_4$ chemical sinks, respectively. S and S_{13} are the total sources of $^{12}CH_4$ and $^{13}CH_4$ (including soil sink as a negative source), respectively.

Let R_{atm}, R_s and $\varepsilon = \alpha - 1 = \frac{k_{13}}{k} - 1$ be the atmospheric isotopic ratio, the source isotopic ratio and the isotopic fractionation coefficient of the total chemical CH_4 sink. We can infer an equation linking these three terms :

$$\frac{dB_{13}}{dt} = S_{13} - k_{13} \cdot B_{13} \tag{S.16}$$

$$\implies \quad \frac{d(R_{\text{atm}} \cdot B)}{dt} = R_s \cdot S - (k \cdot \alpha) \cdot (R_{\text{atm}} \cdot B) \tag{S.17}$$

$$\implies \quad \frac{d(R_{\text{atm}} \cdot B)}{dt} = R_s \cdot S - (1+\varepsilon) \cdot R_{\text{atm}} \cdot P \tag{S.18}$$

Here, $P = k \cdot B$ is the total sink. At steady state, with time derivatives equal to zero, we have :

$$\begin{cases} S - P = 0 \\ R_s \cdot S - (1+\varepsilon) \cdot R_{\text{atm}} \cdot P = 0 \end{cases} \tag{S.19}$$

Subsequently, these equations can be reshaped to obtain a relationship between δ_a, which is the mean atmospheric isotopic composition at steady state, and δ_s, which is the globally-averaged isotopic source signature.

$$R_s \cdot S - (1+\varepsilon) \cdot R_{\text{atm}} \cdot P = 0 \tag{S.20}$$

$$\Longrightarrow \quad R_s - (1+\varepsilon) \cdot R_{\text{atm}} = 0 \tag{S.21}$$

$$\Longrightarrow \quad (1+\delta_s) \cdot R_{std} = (1+\varepsilon) \cdot (1+\delta_a) \cdot R_{std} \tag{S.22}$$

$$\Longrightarrow \quad \delta_a = \frac{1+\delta_s}{1+\varepsilon} - 1 \tag{S.23}$$

With $\delta^{13}\text{C}(\text{CH}_4)$, we have $1+\varepsilon \approx 1$:

$$\delta_a \approx \delta_s - \varepsilon - \delta_s \cdot \varepsilon \tag{S.24}$$

Therefore, the bias $\Delta\delta_a$ between two simulations prescribing the same CH_4 source, the same source signature δ_s but different isotopic fractionations ε is given by the formula :

$$\Delta\delta_a \approx -\Delta\varepsilon \cdot (1+\delta_s) \tag{S.25}$$

Table S1. Prior emissions and flux-weighted isotopic signatures averaged over 1998-2018 for different categories and sub-categories. Values between brackets indicate the minimum and maximum over the time period. * Unc. : Prior uncertainty as a percentage of the grid cell value (or regional value for the signatures) used to fill the matrix **B**.

Categories	Emissions $TgCH_4\ yr^{-1}$	Unc.*	$\delta^{13}C(CH4)_{source}$ ‰ vs PDB	Unc.*
WET	180 [180 / 180]	100 %	-60.8 [-60.8 / -60.8]	10 %
AGW	213 [195 / 232]	100 %	-59.1 [-59.2 / -59.0]	10 %
FFG	117 [99 / 133]	100 %	-44.9 [-45.6 / -44.4]	20 %
BB	27 [24 / 35]	100 %	-22.3 [-22.5 / -22.2]	30 %
NAT	23 [23 / 23]	100 %	-50.7 [-50.7 / -50.7]	15 %

Table S2. Global flux-weighted values and references for $\delta^{13}\mathrm{C}(\mathrm{CH}_4)_{\mathrm{source}}$ source signatures associated to the different emission categories and subcategories. * Values are prescribed at regional or grid cell scale (see Fig. S2).

E19 : (Etiope et al., 2019) ; CH19 : Chang et al. (2019) ; GA18 : Ganesan et al. (2018) ; TH18 : Thompson et al. (2018) ; SH17 : Sherwood et al. (2017) ; SH16 : Schwietzke et al. (2016) ; WA16 : Warwick et al. (2016) ; ZA16 : Zazzeri et al. (2016) ; TO12 : Townsend-Small et al. (2012) ; KL10 : Klevenhusen et al. (2010) ; BO06 : Bousquet et al. (2006) ; BR01 : Bréas et al. (2001) ; SA01 : Sansone et al. (2001) ; CH00 : Chanton et al. (2000) ; HO00 : Holmes et al. (2000) ; CH99 : Chanton et al. (1999) ; BE98 : Bergamaschi et al. (1998) ; LE93 : Levin et al. (1993);

Categories	Global signatures (‰)	Subcategories	Global signature (‰)	References
AGW	-59.1 *	Rice cultivation	-63.0	SH17; BO06; BR01
		Enteric fermentation	-64.7 *	CH19
		Agriculture waste	-52.0	KL10 ; LE93
		Landfills	-52.0	TO12 ; CH99 ; BE98 ; LE93
		Waste water	-48.0	TO12 ; CH99 ; BE98 ; LE93
FFG	-44.9 *	Oil and gas	-44.9 *	SH07
		Coal	-42.3 *	SH07 ; ZA16
		Geological sources	-49	E19
BB	-22.3 *	Biomass burning	-24.9 *	BO06 ; CH00
		Biofuel burning	-20	CH00
WET	-60.8 *	Wetlands	-60.8 *	GA18
NAT	-50.7 *	Oceanic sources	-42	BR01; HO00 ; SA01
		Termites	-63	TH18; SH16 ; SH17; WA16

Table S3. Providers, locations and number of vertical profiles of CH_4 retrieved using AirCore technique between 2012 and 2018. The longitude and latitude given here are means over the AirCore descent profile.

Provider	**Location**	**Number of profiles**	**Longitude**	**Latitude**
NOAA-ESRL Aircraft Program	Edwards AFB/Dryden, USA	6	117.51° W	34.58° N
	Boulder, CO, USA	33	104.34° W	39.53° N
	Lamont, OK, USA	30	97.45° W	36.65° N
	Park Falls, WI, USA	4	90.27° W	46.03° N
	Sodankylä, Finland	6	25.97° E	67.60° N
	Lauder, NZ	1	170.01° E	45.19° S
French AirCore Program	Alice Springs, Australia	3	132.58° E	23.66° S
	Aire-sur-l'Adour, France	9	1.02° E	43.25° N
	Trainou, France	17	1.86° E	47.30° N
	Timmins, Ontario, Canada	4	83.28° W	48.49° N
	Esrange, Northern Sweden	2	22.86° E	67.87° N

Table S4. Balloon flights and number of samples analyzed for $\delta^{13}C(CH_4)$ vertical profiles. Each flight is given a flight ID as STA-JJ-MM, where STA is the 3-letter-code for the balloon launch station, JJ the year and MM the month of sampling. This Table is adapted from Röckmann et al. (2011). [1] HYD: Hyderabad, India (17.5 °N, 78.60 °E); [2] KIR: Kiruna, Sweden (67.9 °N, 21.10 °E); [3] ASA: Aire sur l'Adour, France (43.70 °N, - 0.30 °E); [4] GAP: Gap, France (44.44 °N, 6.14 °E);

Flight ID	Flight Date	Location	Number of $\delta^{13}C(CH_4)$ samples	Characteristics
Flights operated by MPI für Sonnensystemforschung				
HYD-99-04	04/29/99	HYD[1]	10	Subtropical
GAP-99-06	06/23/99	GAP[4]	15	Mid-latitudinal summer
Flights operated by Institut für Meteorologie und Geophysik, Universität Frankfurt				
KIR-00-01	01/03/00	KIR[2]	13	Artic strong vortex
ASA-01-10	10/11/01	ASA[3]	13	Mid-latitudinal background
ASA-02-09	09/15/02	ASA[3]	13	Mid-latitudinal background
KIR-03-03	03/06/03	KIR[2]	13	Arctic vortex, mesospheric enclosure
KIR-03-03	06/09/03	KIR[2]	13	Artic summer

Table S5. List of CH_4 surface in-situ observation sites that provided measurements assimilated in the inversion between 1998 and 2018. AOC, PAO, POC et WPC are mobile stations. Their characteristics are compiled into a single line, providing latitude and longitude ranges of the measurements. Stations that retrieved samples consisting mainly of well-mixed Marine Boundary Layer (MBL) air are indicated in bold red.

Site code	Station name	Country/Territory	Network	Latitude	Longitude	Elevation (m a.s.l.)	Date range (MM/YYYY)
ABP	Arembepe	Brazil	NOAA	12.76° S	38.16° W	6	10/2006 - 01/2010
ALT	Alert	Canada	NOAA	82.45° N	62.51° W	195	01/1998 - 12/2018
AMT	Argyle	United States	NOAA	45.03° N	68.68° W	157	09/2003 - 12/2008
AMY	Anmyeon-do	Republic of Korea	NOAA	36.54° N	126.33° E	125	12/2013 - 12/2018
AOC	Atlantic Ocean Cruise	N/A	NOAA	30.30° S 35.00° N	-75.11° W 13.57° E	22	05/2004 - 02/2005
ASC	Ascension Island	United Kingdom	NOAA	7.97° S	14.40° W	90	01/1998 - 12/2018
ASK	Assekrem	Algeria	NOAA	23.26° N	5.63° E	2715	01/1998 - 12/2018
AZR	Terceira Island	Portugal	NOAA	38.77° N	27.38° W	24	01/1998 - 12/2018
BAL	Baltic Sea	Poland	NOAA	55.43° N	16.95° E	28	01/1998 - 06/2011
BHD	Baring Head Station	New Zealand	NOAA	41.41° S	174.87° E	90	10/1999 - 12/2018
BKT	Bukit Kototabang	Indonesia	NOAA	0.20° S	100.32° E	875	01/2004 - 12/2018
BME	St. Davids Head	United Kingdom	NOAA	32.37° N	64.65° W	17	01/1998 - 01/2010
BMW	Tudor Hill	United Kingdom	NOAA	32.26° N	64.88° W	60	01/1998 - 12/2018
BRW	Barrow Atmospheric Baseline Observatory	United States	NOAA	71.32° N	156.60° W	13	01/1998 - 12/2018
BSC	Black Sea	Romania	NOAA	44.18° N	28.66° E	5	01/1998 - 12/2011
CBA	Cold Bay	United States	NOAA	55.20° N	162.72° W	25	01/1998 - 12/2018
CGO	Cape Grim	Australia	NOAA	40.68° S	144.68° E	164	01/1998 - 12/2018
CHR	Christmas Island	Republic of Kiribati	NOAA	1.70° N	157.15° W	5	11/1998 - 12/2018
CIB	Centro de Investigacion de la Baja Atmosfera (CIBA)	Spain	NOAA	41.81° N	4.93° W	850	05/2009 - 12/2018
CMO	Cape Meares	United States	NOAA	45.48° N	123.97° W	35	03/1998 - 03/1998
CPT	Cape Point	South Africa	NOAA	34.35° S	18.49° E	260	02/2010 - 12/2018
CRZ	Crozet Island	France	NOAA	46.43° S	51.85° E	202	01/1998 - 11/2018
DRP	Drake Passage	nan	NOAA	57.65° S	64.18° W	10	04/2003 - 12/2018
DSI	Dongsha Island	Taiwan	NOAA	20.70° N	116.73° E	8	03/2010 - 12/2018
EIC	Easter Island	Chile	NOAA	27.15° S	109.45° W	55	01/1998 - 12/2018
GMI	Mariana Islands	Guam	NOAA	13.39° N	144.66° E	6	01/1998 - 12/2018
GOZ	Dwejra Point	Malta	NOAA	36.05° N	14.89° E	6	01/1998 - 02/1999
HBA	Halley Station	United Kingdom	NOAA	75.61° S	26.21° W	35	01/1998 - 02/2018
HPB	Hohenpeissenberg	Germany	NOAA	47.80° N	11.02° E	990	04/2006 - 12/2018
HSU	Humboldt State University	United States	NOAA	41.05° N	124.73° W	7	05/2008 - 05/2017

Table S5. Following Table S5

Site code	Station name	Country/Territory	Network	Latitude	Longitude	Elevation (m a.s.l.)	Date range (MM/YYYY)
HUN	Hegyhatsal	Hungary	NOAA	46.95° N	16.65° E	344	01/1998 - 12/2018
ICE	Storhofdi	Iceland	NOAA	63.40° N	20.29° W	127	01/1998 - 12/2018
ITN	Grifton	United States	NOAA	35.37° N	77.39° W	505	01/1998 - 06/1999
IZO	Izana	Spain	NOAA	28.30° N	16.48° W	2377	01/1998 - 12/2018
KCO	Kaashidhoo	Republic of Maldives	NOAA	4.97° N	73.47° E	6	03/1998 - 07/1999
KEY	Key Biscayne	United States	NOAA	25.67° N	80.20° W	6	01/1998 - 12/2018
KUM	Cape Kumukahi	United States	NOAA	19.52° N	154.82° W	8	01/1998 - 12/2018
KZD	Sary Taukum	Kazakhstan	NOAA	44.45° N	75.57° E	412	01/1998 - 08/2009
KZM	Plateau Assy	Kazakhstan	NOAA	43.25° N	77.88° E	2524	01/1998 - 08/2009
LEF	Park Falls	United States	NOAA	45.93° N	90.27° W	868	01/1998 - 12/2018
LLB	Lac La Biche	Canada	NOAA	54.95° N	112.45° W	546	01/2008 - 02/2013
LLN	Lulin	Taiwan	NOAA	23.46° N	120.86° E	2867	08/2006 - 12/2018
LMP	Lampedusa	Italy	NOAA	35.51° N	12.61° E	50	10/2006 - 12/2018
MEX	High Altitude Global Climate Observation Center	Mexico	NOAA	18.98° N	97.31° W	4469	01/2009 - 12/2018
MHD	Mace Head	Ireland	NOAA	53.33° N	9.90° W	26	01/1998 - 12/2018
MID	Sand Island	United States	NOAA	28.22° N	177.37° W	8	01/1998 - 12/2018
MKN	Mt. Kenya	Kenya	NOAA	0.06° S	37.30° E	3649	12/2003 - 06/2011
MLO	Mauna Loa	United States	NOAA	19.53° N	155.58° W	3437	01/1998 - 12/2018
NAT	Farol De Mae Luiza Lighthouse	Brazil	NOAA	5.51° S	35.26° W	20	09/2010 - 12/2018
NMB	Gobabeb	Namibia	NOAA	23.58° S	15.03° E	461	07/1998 - 12/2018
NWR	Niwot Ridge	United States	NOAA	40.05° N	105.58° W	3526	01/1998 - 12/2018
OXK	Ochsenkopf	Germany	NOAA	50.03° N	11.81° E	1185	03/2003 - 12/2018
PAL	Pallas-Sammaltunturi	Finland	NOAA	67.97° N	24.12° E	570	12/2001 - 12/2018
PAO	Pacific-Atlantic Ocean	N/A	NOAA	30.20° S 67.86° N	164.58° W 9.93° W	10	03/2006 - 10/2006
POC	Pacific Ocean	N/A	NOAA	36.67° S 35.07° N	180.00° W 179.83° E	20	04/1998 - 07/2017
PSA	Palmer Station	United States	NOAA	64.92° S	64.00° W	15	01/1998 - 12/2018
PTA	Point Arena	United States	NOAA	38.95° N	123.73° W	22	01/1999 - 05/2011
RPB	Ragged Point	Barbados	NOAA	13.16° N	59.43° W	20	01/1998 - 12/2018
SDZ	Shangdianzi	Peoples Republic of China	NOAA	40.65° N	117.12° E	298	09/2009 - 09/2015
SEY	Mahe Island	Seychelles	NOAA	4.68° S	55.53° E	7	01/1998 - 12/2018

Table S5. Following Table S5

Site code	Station name	Country/Territory	Network	Latitude	Longitude	Elevation (m a.s.l.)	Date range (MM/YYYY)
SGP	Southern Great Plains	United States	NOAA	36.62° N	97.48° W	374	04/2002 - 12/2018
SHM	Shemya Island	United States	NOAA	52.72° N	174.10° E	28	01/1998 - 10/2018
SMO	Tutuila	American Samoa	NOAA	14.25° S	170.57° W	47	01/1998 - 12/2018
SPO	South Pole	United States	NOAA	89.98° S	24.80° W	2821	01/1998 - 12/2018
STM	Ocean Station M	Norway	NOAA	66.00° N	2.00° E	7	01/1998 - 11/2009
SUM	Summit	Greenland	NOAA	72.60° N	38.42° W	3214	01/1998 - 12/2018
SYO	Syowa Station	Japan	NOAA	69.00° S	39.58° E	16	01/1998 - 12/2018
TAC	Tacolneston	United Kingdom	NOAA	52.52° N	1.14° E	236	06/2014 - 01/2016
TAP	Tae-ahn Peninsula	Republic of Korea	NOAA	36.73° N	126.13° E	21	01/1998 - 12/2018
THD	Trinidad Head	United States	NOAA	41.05° N	124.15° W	112	04/2002 - 06/2017
TIK	Hydrometeorological Observatory of Tiksi	Russia	NOAA	71.60° N	128.89° E	29	08/2011 - 09/2018
USH	Ushuaia	Argentina	NOAA	54.85° S	68.31° W	32	01/1998 - 12/2018
UTA	Wendover	United States	NOAA	39.90° N	113.72° W	1332	01/1998 - 12/2018
UUM	Ulaan Uul	Mongolia	NOAA	44.45° N	111.10° E	1012	01/1998 - 12/2018
WIS	Weizmann Institute of Science at the Arava Institute	Israel	NOAA	30.86° N	34.78° E	482	01/1998 - 12/2018
WKT	Moody	United States	NOAA	31.32° N	97.33° W	708	02/2001 - 10/2010
WLG	Mt. Waliguan	Peoples Republic of China	NOAA	36.27° N	100.92° E	3815	01/1998 - 12/2018
WPC	Western Pacific Cruise	N/A	NOAA	30.67° S 32.46° N	135.55° E 170.47° E	8	05/2004 - 06/2013
ZEP	Ny-Alesund	Norway and Sweden	NOAA	78.91° N	11.89° E	479	01/1998 - 12/2018

Table S6. List of $\delta^{13}\mathrm{C}(\mathrm{CH_4})$ surface in-situ observation sites that provided measurements assimilated in the inversion between 1998 and 2018. WPC is a mobile station. Its characteristics are compiled into a single line, providing latitude and longitude ranges of the measurements. Stations that retrieved samples consisting mainly of well-mixed MBL air are indicated in bold red.

Site code	Station name	Country/Territory	Network	Latitude	Longitude	Elevation (m a.s.l.)	Date range (MM/YYYY)
ALT	Alert	Canada	NOAA	82.45° N	62.51° W	195	08/2000 - 12/2017
AMY	Anmyeon-do	Republic of Korea	NOAA	36.54° N	126.33° E	125	12/2013 - 12/2017
ASC	Ascension Island	United Kingdom	NOAA	7.97° S	14.40° W	90	10/2000 - 12/2017
AZR	Terceira Island	Portugal	NOAA	38.75° N	27.08° W	24	08/2000 - 12/2017
BAL	Baltic Sea	Poland	NOAA	55.35° N	17.22° E	28	04/2008 - 06/2011
BHD	Baring Head Station	New Zealand	NOAA	41.41° S	174.87° E	90	03/2009 - 11/2017
BRW	Barrow Atmospheric Baseline Observatory	United States	NOAA	71.32° N	156.60° W	16	01/1998 - 12/2017
CBA	Cold Bay	United States	NOAA	55.20° N	162.72° W	25	08/2000 - 12/2017
CGO	Cape Grim	Australia	NOAA	40.68° S	144.68° E	164	01/1998 - 12/2017
KUM	Cape Kumukahi	United States	NOAA	19.52° N	154.82° W	3	01/1999 - 12/2017
LLB	Lac La Biche	Canada	NOAA	54.95° N	112.45° W	546	01/2008 - 02/2013
MEX	High Altitude Global Climate Observation Center	Mexico	NOAA	18.98° N	97.31° W	4469	01/2009 - 12/2017
MHD	Mace Head	Ireland	NOAA	53.33° N	9.90° W	26	01/1999 - 12/2017
MLO	Mauna Loa	United States	NOAA	19.53° N	155.58° W	3402	01/1998 - 12/2017
NWR	Niwot Ridge	United States	NOAA	40.05° N	105.58° W	3526	01/1998 - 12/2017
SMO	Tutuila	American Samoa	NOAA	14.25° S	170.57° W	47	01/1998 - 12/2017
SPO	South Pole	United States	NOAA	89.98° S	24.80° W	2815	01/1998 - 12/2017
SUM	Summit	Greenland	NOAA	72.60° N	38.42° W	3214	04/2010 - 12/2017
TAP	Tae-ahn Peninsula	Republic of Korea	NOAA	36.73° N	126.13° E	21	09/2000 - 12/2017
WLG	Mt. Waliguan	Peoples Republic of China	NOAA	36.27° N	100.92° E	3815	07/2001 - 12/2017
WPC	Western Pacific Cruise	N/A	NOAA	30.35° S	167.73° E	10	11/2005 - 06/2013
ZEP	Ny-Alesund	Norway and Sweden	NOAA	78.91° N	11.89° E	479	10/2001 - 12/2017

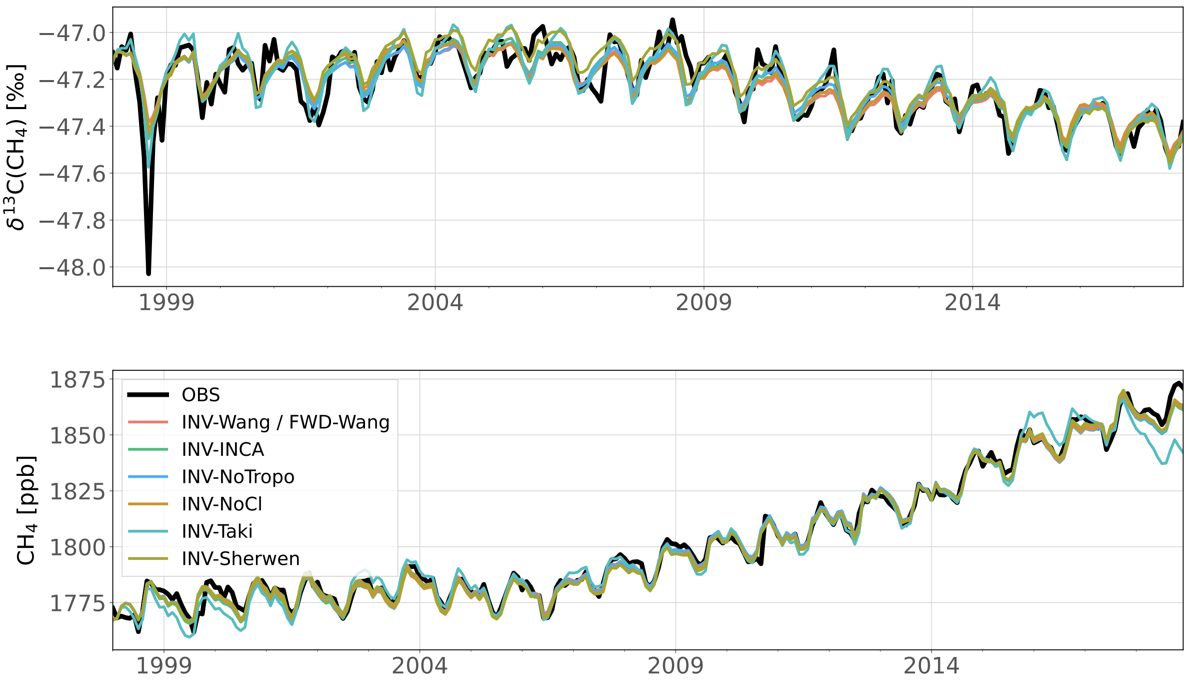

Figure S1. Time-series of observed and simulated CH_4 and $\delta^{13}C(CH_4)$ monthly values averaged over the globe using a latitudinal band average (30°)

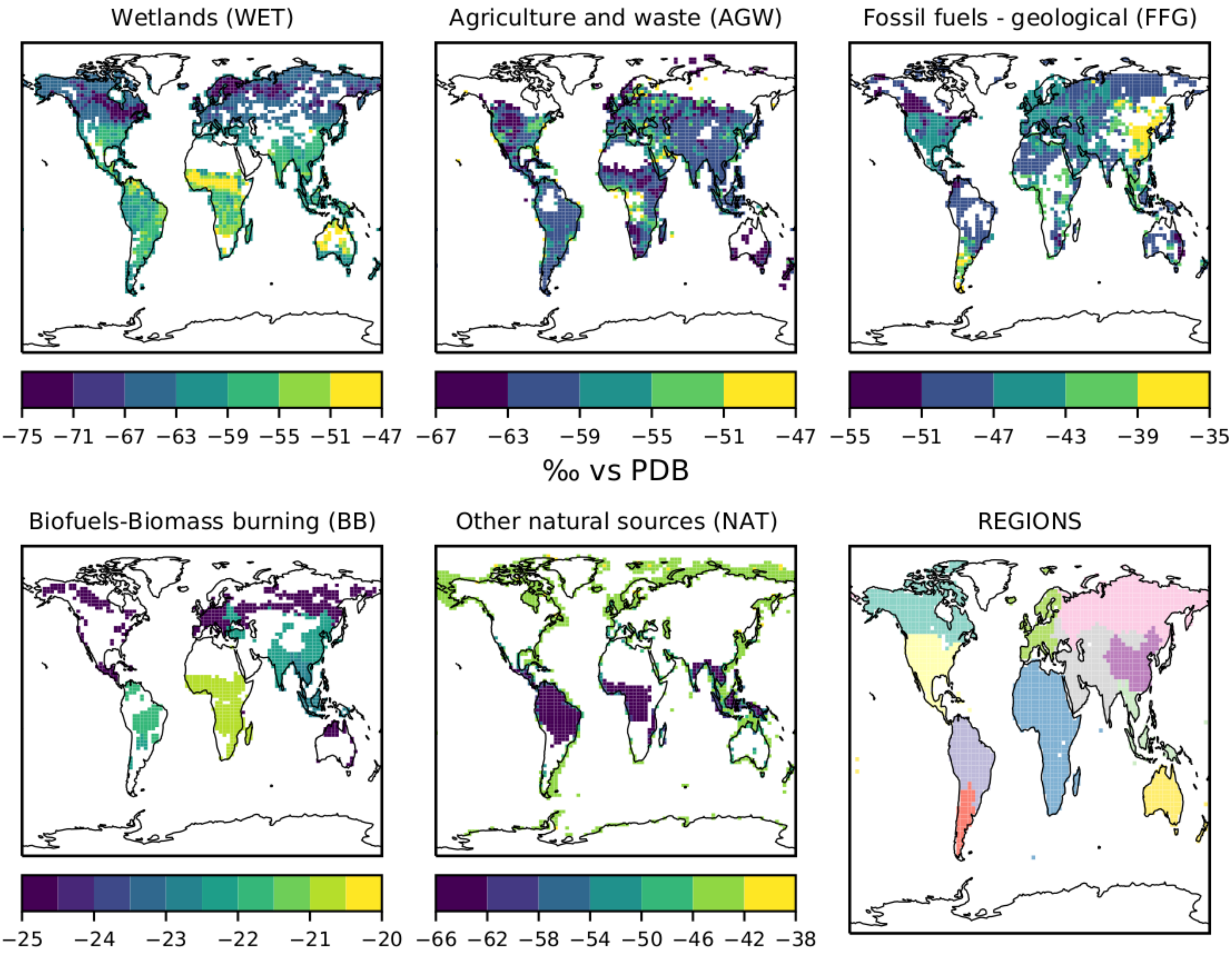

Figure S2. Prior estimates of $\delta^{13}C(CH_4)_{source}$ isotopic signatures for each of the five emission categories averaged over the 1998-2018 period. The regions over which the values are optimized are shown in the lower-right panel. WET source signatures are dependent on the latitude, with more depleted values in boreal regions than in tropical regions. BB source signatures are dependent on the vegetation (C3/C4). Burning C4 vegetation tropical regions releases CH_4 that is more ^{13}C-enriched than CH_4 released when burning C3 vegetation. AGW source signatures is dependent on the country/region and the C3 versus C4 livestock diet. FFG source signatures mainly depend both on the location and the contributions from coal, oil&gas and geological sources to the total FFG emissions of a specific country/region. For example, China ^{13}C-enriched large coal emissions highly contributes to the FFG source signature in this region which is notably ^{13}C-enriched compared to other regions.

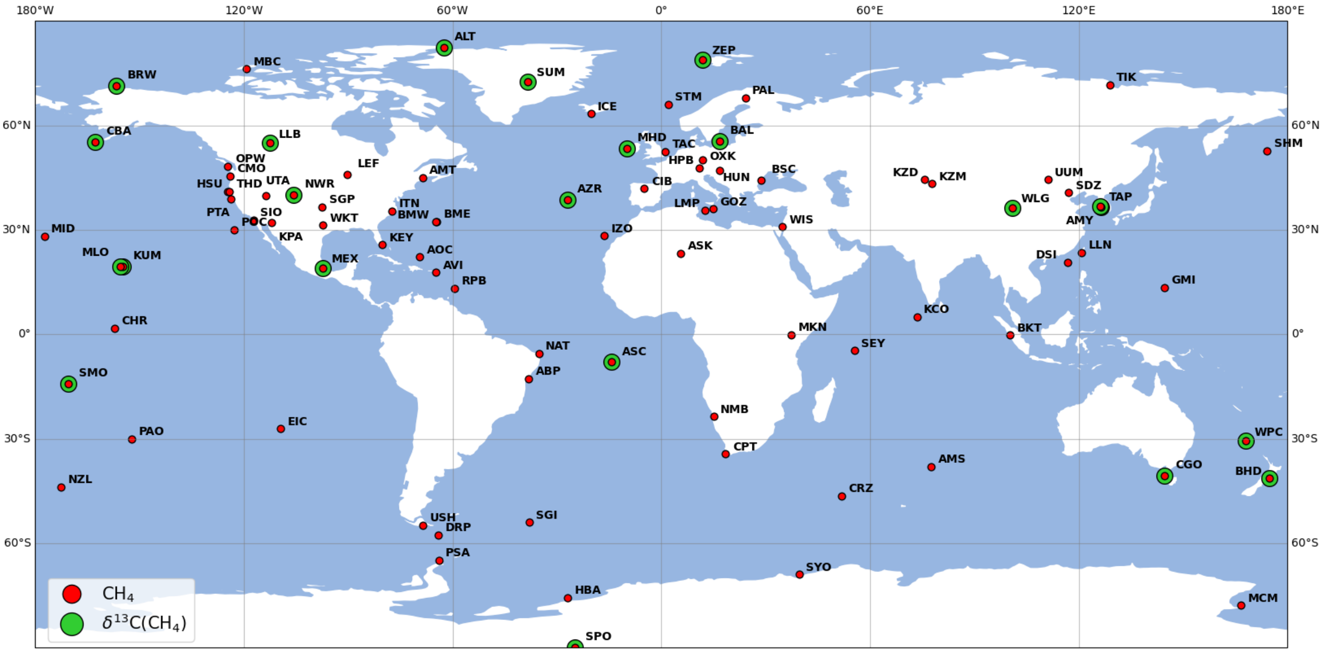

Figure S3. Locations of CH_4 and $\delta^{13}C(CH_4)$ surface stations. Affiliated networks are not displayed. More information about the stations can be found in Table S5 and Table S6.

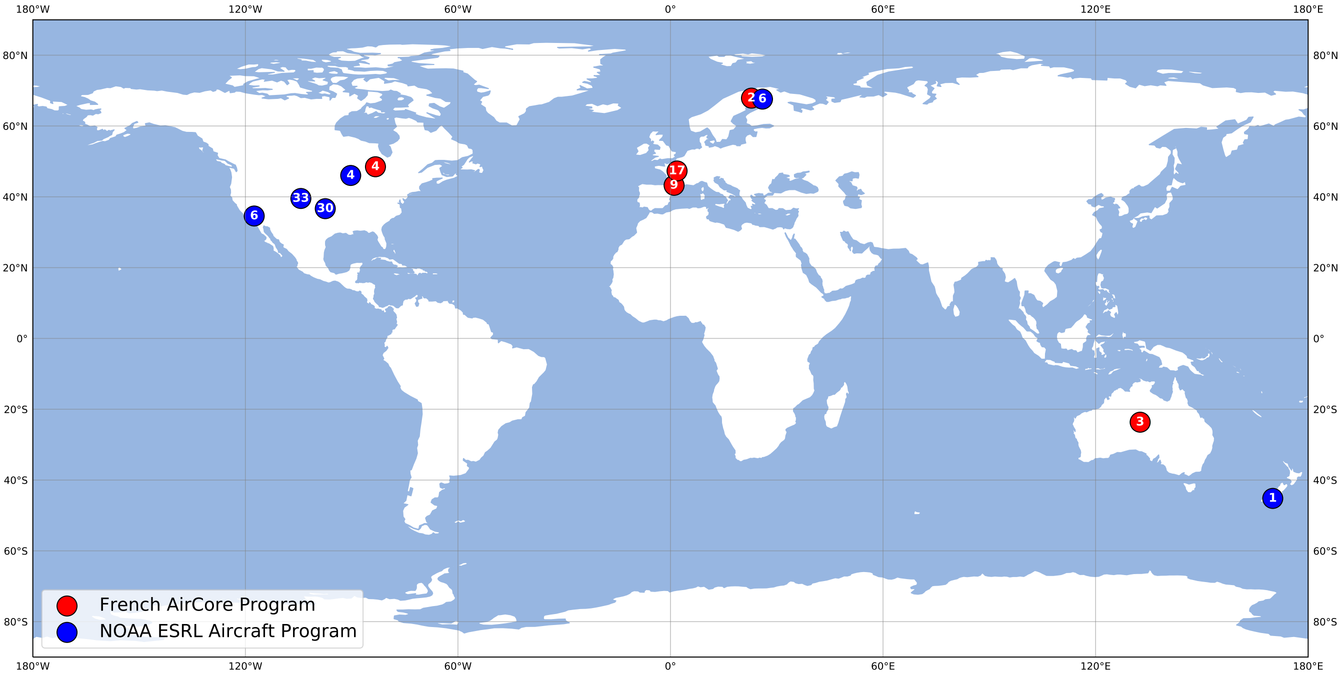

Figure S4. Locations and numbers of CH_4 vertical profiles retrieved using the AirCore technique. A comprehensive list of locations and associated providers can be found in Table S3.

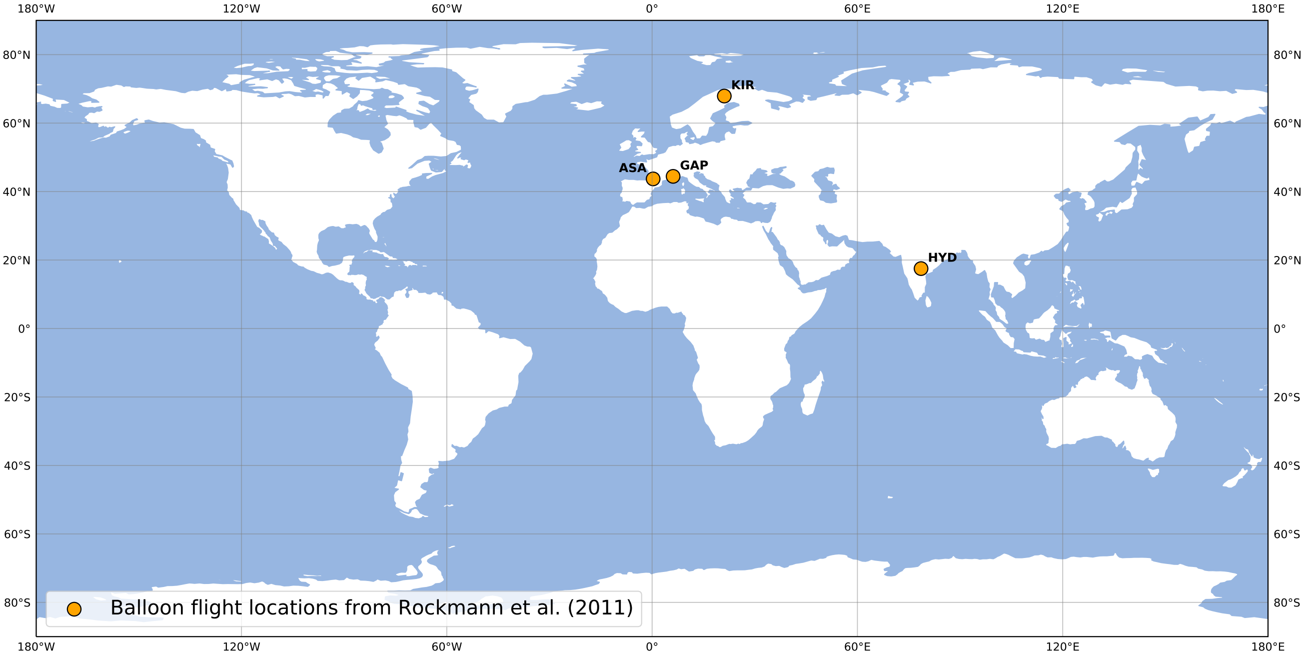

Figure S5. Locations and numbers of $\delta^{13}\mathrm{C}(\mathrm{CH}_4)$ vertical profiles provided by Röckmann et al. (2011). A comprehensive list of locations can be found in Table S4.

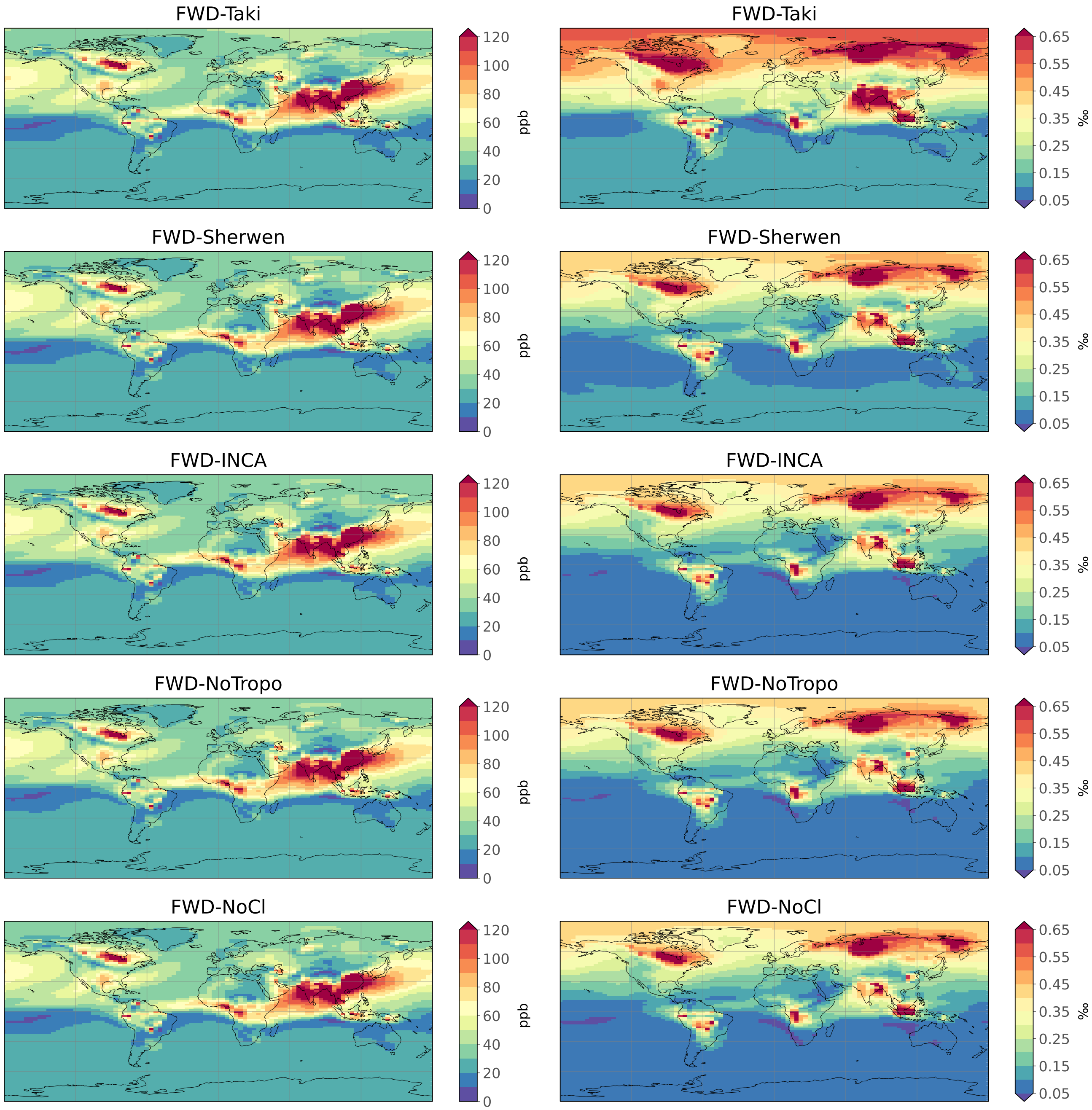

Figure S6. Mean seasonal cycles for multiple sensitivity tests averaged over 1998-2018. Left panels show the peak-to-peak amplitudes of the CH_4 seasonal cycle. Right panels show the peak-to-peak amplitudes of the $\delta^{13}C(CH_4)$ seasonal cycle. For clarity reasons and as all seasonal cycles are here very similar, the FWD-Wang seasonal cycle amplitudes are not displayed. Note that colour scales are identical for all simulations.

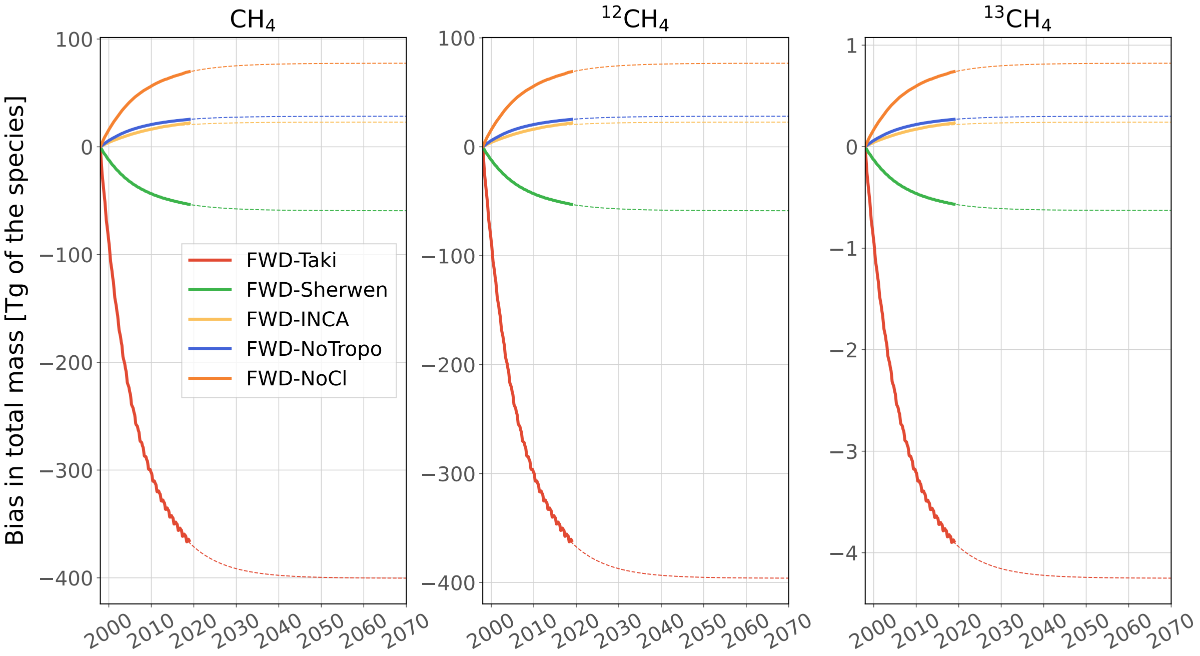

Figure S7. Biases in total atmospheric masses for CH_4, $^{12}CH_4$ and $^{13}CH_4$ between FWD-* and FWD-Wang. Solid lines correspond to the monthly simulated values. Dashed lines correspond to the extended values following the methods in Sect. S2.

References

Berchet, A., Sollum, E., Thompson, R. L., Pison, I., Thanwerdas, J., Broquet, G., Chevallier, F., Aalto, T., Berchet, A., Bergamaschi, P., Brunner, D., Engelen, R., Fortems-Cheiney, A., Gerbig, C., Groot Zwaaftink, C. D., Haussaire, J.-M., Henne, S., Houweling, S., Karstens, U., Kutsch, W. L., Luijkx, I. T., Monteil, G., Palmer, P. I., van Peet, J. C. A., Peters, W., Peylin, P., Potier, E., Rödenbeck, C., Saunois, M., Scholze, M., Tsuruta, A., and Zhao, Y.: The Community Inversion Framework v1.0: a unified system for atmospheric inversion studies, Geoscientific Model Development, 14, 5331–5354, https://doi.org/10.5194/gmd-14-5331-2021, 2021.

Bergamaschi, P., Lubina, C., Königstedt, R., Fischer, H., Veltkamp, A. C., and Zwaagstra, O.: Stable isotopic signatures (δ^{13}C, δD) of methane from European landfill sites, Journal of Geophysical Research: Atmospheres, 103, 8251–8265, https://doi.org/10.1029/98JD00105, 1998.

Bousquet, P., Ciais, P., Miller, J. B., Dlugokencky, E. J., Hauglustaine, D. A., Prigent, C., Van der Werf, G. R., Peylin, P., Brunke, E.-G., Carouge, C., Langenfelds, R. L., Lathière, J., Papa, F., Ramonet, M., Schmidt, M., Steele, L. P., Tyler, S. C., and White, J.: Contribution of anthropogenic and natural sources to atmospheric methane variability, Nature, 443, 439–443, https://doi.org/10.1038/nature05132, 2006.

Bréas, O., Guillou, C., Reniero, F., and Wada, E.: The Global Methane Cycle: Isotopes and Mixing Ratios, Sources and Sinks, Isotopes in Environmental and Health Studies, 37, 257–379, https://doi.org/10.1080/10256010108033302, 2001.

Chang, J., Peng, S., Ciais, P., Saunois, M., Dangal, S. R. S., Herrero, M., Havlík, P., Tian, H., and Bousquet, P.: Revisiting enteric methane emissions from domestic ruminants and their $\delta^{13}C_{CH4}$ source signature, Nature Communications, 10, 3420, https://doi.org/10.1038/s41467-019-11066-3, 2019.

Chanton, J. P., Rutkowski, C. M., and Mosher, B.: Quantifying Methane Oxidation from Landfills Using Stable Isotope Analysis of Downwind Plumes, Environmental Science & Technology, 33, 3755–3760, https://doi.org/10.1021/es9904033, 1999.

Chanton, J. P., Rutkowski, C. M., Schwartz, C. C., Ward, D. E., and Boring, L.: Factors influencing the stable carbon isotopic signature of methane from combustion and biomass burning, Journal of Geophysical Research: Atmospheres, 105, 1867–1877, https://doi.org/10.1029/1999JD900909, 2000.

Cressot, C., Chevallier, F., Bousquet, P., Crevoisier, C., Dlugokencky, E. J., Fortems-Cheiney, A., Frankenberg, C., Parker, R., Pison, I., Scheepmaker, R. A., Montzka, S. A., Krummel, P. B., Steele, L. P., and Langenfelds, R. L.: On the consistency between global and regional methane emissions inferred from SCIAMACHY, TANSO-FTS, IASI and surface measurements, Atmospheric Chemistry and Physics, 14, 577–592, https://doi.org/10.5194/acp-14-577-2014, 2014.

Etiope, G.: Natural Gas Seepage: The Earth's Hydrocarbon Degassing, Springer International Publishing, www.springer.com/gp/book/9783319146003, 2015.

Etiope, G., Ciotoli, G., Schwietzke, S., and Schoell, M.: Gridded maps of geological methane emissions and their isotopic signature, https://doi.org/10.5194/essd-11-1-2019, 2019.

Feinberg, A. I., Coulon, A., Stenke, A., Schwietzke, S., and Peter, T.: Isotopic source signatures: Impact of regional variability on the $\delta^{13}C(CH_4)$ trend and spatial distribution, Atmospheric Environment, 174, 99–111, https://doi.org/10.1016/j.atmosenv.2017.11.037, 2018.

Ganesan, A. L., Stell, A. C., Gedney, N., Comyn-Platt, E., Hayman, G., Rigby, M., Poulter, B., and Hornibrook, E. R. C.: Spatially Resolved Isotopic Source Signatures of Wetland Methane Emissions, Geophysical Research Letters, 45, 3737–3745, https://doi.org/10.1002/2018GL077536, 2018.

Gilbert, J. C. and Lemaréchal, C.: Some numerical experiments with variable-storage quasi-Newton algorithms, Mathematical Programming, 45, 407–435, https://doi.org/10.1007/BF01589113, 1989.

Hauglustaine, D. A., Hourdin, F., Jourdain, L., Filiberti, M.-A., Walters, S., Lamarque, J.-F., and Holland, E. A.: Interactive chemistry in the Laboratoire de Météorologie Dynamique general circulation model: Description and background tropospheric chemistry evaluation, Journal of Geophysical Research: Atmospheres, 109, https://doi.org/10.1029/2003JD003957, 2004.

Holmes, M. E., Sansone, F. J., Rust, T. M., and Popp, B. N.: Methane production, consumption, and air-sea exchange in the open ocean: An Evaluation based on carbon isotopic ratios, Global Biogeochemical Cycles, 14, 1–10, https://doi.org/10.1029/1999GB001209, 2000.

Ide, K., Courtier, P., Ghil, M., and Lorenc, A. C.: Unified Notation for Data Assimilation : Operational, Sequential and Variational (gtSpecial IssueltData Assimilation in Meteology and Oceanography: Theory and Practice), Journal of the Meteorological Society of Japan. Ser. II, 75, 181–189, https://doi.org/10.2151/jmsj1965.75.1B_181, 1997.

Janssens-Maenhout, G., Crippa, M., Guizzardi, D., Muntean, M., Schaaf, E., Dentener, F., Bergamaschi, P., Pagliari, V., Olivier, J. G. J., Peters, J. A. H. W., van Aardenne, J. A., Monni, S., Doering, U., Petrescu, A. M. R., Solazzo, E., and Oreggioni, G. D.: EDGAR v4.3.2 Global Atlas of the three major greenhouse gas emissions for the period 1970–2012, Earth System Science Data, 11, 959–1002, https://doi.org/10.5194/essd-11-959-2019, 2019.

Kirschke, S., Bousquet, P., Ciais, P., Saunois, M., Canadell, J. G., Dlugokencky, E. J., Bergamaschi, P., Bergmann, D., Blake, D. R., Bruhwiler, L., Cameron-Smith, P., Castaldi, S., Chevallier, F., Feng, L., Fraser, A., Heimann, M., Hodson, E. L., Houweling, S., Josse, B., Fraser, P. J., Krummel, P. B., Lamarque, J.-F., Langenfelds, R. L., Le Quéré, C., Naik, V., O'Doherty, S., Palmer, P. I., Pison, I., Plummer, D., Poulter, B., Prinn, R. G., Rigby, M., Ringeval, B., Santini, M., Schmidt, M., Shindell, D. T., Simpson, I. J., Spahni, R., Steele, L. P., Strode, S. A., Sudo, K., Szopa, S., van der Werf, G. R., Voulgarakis, A., van Weele, M., Weiss, R. F., Williams, J. E., and Zeng, G.: Three decades of global methane sources and sinks, Nature Geoscience, 6, 813–823, https://doi.org/10.1038/ngeo1955, 2013.

Klevenhusen, F., Bernasconi, S. M., Kreuzer, M., and Soliva, C. R.: Experimental validation of the Intergovernmental Panel on Climate Change default values for ruminant-derived methane and its carbon-isotope signature, Animal Production Science, 50, 159, https://doi.org/10.1071/AN09112, 2010.

Lambert, G. and Schmidt, S.: Reevaluation of the oceanic flux of methane: Uncertainties and long term variations, Chemosphere, 26, 579–589, https://doi.org/10.1016/0045-6535(93)90443-9, 1993.

Levin, I., Bergamaschi, P., Dörr, H., and Trapp, D.: Stable isotopic signature of methane from major sources in Germany, Chemosphere, 26, 161–177, https://doi.org/10.1016/0045-6535(93)90419-6, 1993.

Locatelli, R., Bousquet, P., Chevallier, F., Fortems-Cheney, A., Szopa, S., Saunois, M., Agusti-Panareda, A., Bergmann, D., Bian, H., Cameron-Smith, P., Chipperfield, M. P., Gloor, E., Houweling, S., Kawa, S. R., Krol, M., Patra, P. K., Prinn, R. G., Rigby, M., Saito, R., and Wilson, C.: Impact of transport model errors on the global and regional methane emissions estimated by inverse modelling, Atmospheric Chemistry and Physics, 13, 9917–9937, https://doi.org/doi.org/10.5194/acp-13-9917-2013, 2013.

Locatelli, R., Bousquet, P., Saunois, M., Chevallier, F., and Cressot, C.: Sensitivity of the recent methane budget to LMDz sub-grid-scale physical parameterizations, Atmospheric Chemistry and Physics, 15, 9765–9780, https://doi.org/10.5194/acp-15-9765-2015, 2015.

Masarie, K. A. and Tans, P. P.: Extension and integration of atmospheric carbon dioxide data into a globally consistent measurement record, Journal of Geophysical Research: Atmospheres, 100, 11 593–11 610, https://doi.org/10.1029/95JD00859, 1995.

Patra, P. K., Krol, M. C., Montzka, S. A., Arnold, T., Atlas, E. L., Lintner, B. R., Stephens, B. B., Xiang, B., Elkins, J. W., Fraser, P. J., Ghosh, A., Hintsa, E. J., Hurst, D. F., Ishijima, K., Krummel, P. B., Miller, B. R., Miyazaki, K., Moore, F. L., Mühle, J., O'Doherty, S., Prinn, R. G., Steele, L. P., Takigawa, M., Wang, H. J., Weiss, R. F., Wofsy, S. C., and Young, D.: Observational evidence for interhemispheric hydroxyl-radical parity, Nature, 513, 219–223, https://doi.org/10.1038/nature13721, 2014.

Poulter, B., Bousquet, P., Canadell, J. G., Ciais, P., Peregon, A., Saunois, M., Arora, V. K., Beerling, D. J., Brovkin, V., Jones, C. D., Joos, F., Gedney, N., Ito, A., Kleinen, T., Koven, C. D., McDonald, K., Melton, J. R., Peng, C., Peng, S., Prigent, C., Schroeder, R., Riley, W. J., Saito, M., Spahni, R., Tian, H., Taylor, L., Viovy, N., Wilton, D., Wiltshire, A., Xu, X., Zhang, B., Zhang, Z., and Zhu, Q.: Global wetland contribution to 2000–2012 atmospheric methane growth rate dynamics, Environmental Research Letters, 12, 094 013, https://doi.org/10.1088/1748-9326/aa8391, 2017.

Prather, M. J., Holmes, C. D., and Hsu, J.: Reactive greenhouse gas scenarios: Systematic exploration of uncertainties and the role of atmospheric chemistry: ATMOSPHERIC CHEMISTRY AND GREENHOUSE GASES, Geophysical Research Letters, 39, n/a–n/a, https://doi.org/10.1029/2012GL051440, 2012.

Quay, P., Stutsman, J., Wilbur, D., Snover, A., Dlugokencky, E., and Brown, T.: The isotopic composition of atmospheric methane, Global Biogeochemical Cycles, 13, 445–461, https://doi.org/10.1029/1998GB900006, 1999.

Rayner, P. J., Michalak, A. M., and Chevallier, F.: Fundamentals of data assimilation applied to biogeochemistry, Atmospheric Chemistry and Physics, 19, 13 911–13 932, https://doi.org/10.5194/acp-19-13911-2019, 2019.

Rodenbeck, C., Houweling, S., Gloor, M., and Heimann, M.: CO_2 flux history 1982–2001 inferred from atmospheric data using a global inversion of atmospheric transport, Atmos. Chem. Phys., p. 46, 2003.

Röckmann, T., Brass, M., Borchers, R., and Engel, A.: The isotopic composition of methane in the stratosphere: high-altitude balloon sample measurements, Atmospheric Chemistry and Physics, 11, 13 287–13 304, https://doi.org/doi.org/10.5194/acp-11-13287-2011, 2011.

Sansone, F. J., Popp, B. N., Gasc, A., Graham, A. W., and Rust, T. M.: Highly elevated methane in the eastern tropical North Pacific and associated isotopically enriched fluxes to the atmosphere, Geophysical Research Letters, 28, 4567–4570, https://doi.org/10.1029/2001GL013460, 2001.

Saunois, M., Stavert, A. R., Poulter, B., Bousquet, P., Canadell, J. G., Jackson, R. B., Raymond, P. A., Dlugokencky, E. J., Houweling, S., Patra, P. K., Ciais, P., Arora, V. K., Bastviken, D., Bergamaschi, P., Blake, D. R., Brailsford, G., Bruhwiler, L., Carlson, K. M., Carrol, M., Castaldi, S., Chandra, N., Crevoisier, C., Crill, P. M., Covey, K., Curry, C. L., Etiope, G., Frankenberg, C., Gedney, N., Hegglin, M. I., Höglund-Isaksson, L., Hugelius, G., Ishizawa, M., Ito, A., Janssens-Maenhout, G., Jensen, K. M., Joos, F., Kleinen, T., Krummel, P. B., Langenfelds, R. L., Laruelle, G. G., Liu, L., Machida, T., Maksyutov, S., McDonald, K. C., McNorton, J., Miller, P. A., Melton, J. R., Morino, I., Müller, J., Murguia-Flores, F., Naik, V., Niwa, Y., Noce, S., O'Doherty, S., Parker, R. J., Peng, C., Peng, S., Peters, G. P., Prigent, C., Prinn, R., Ramonet, M., Regnier, P., Riley, W. J., Rosentreter, J. A., Segers, A., Simpson, I. J., Shi, H., Smith, S. J., Steele, L. P., Thornton, B. F., Tian, H., Tohjima, Y., Tubiello, F. N., Tsuruta, A., Viovy, N., Voulgarakis, A., Weber, T. S., van Weele, M., van der Werf, G. R., Weiss, R. F., Worthy, D., Wunch, D., Yin, Y., Yoshida, Y., Zhang, W., Zhang, Z., Zhao, Y., Zheng, B., Zhu, Q., Zhu, Q., and Zhuang, Q.: The Global Methane Budget 2000–2017, Earth System Science Data, 12, 1561–1623, https://doi.org/doi.org/10.5194/essd-12-1561-2020, 2020.

Schwietzke, S., Sherwood, O. A., Bruhwiler, L. M. P., Miller, J. B., Etiope, G., Dlugokencky, E. J., Michel, S. E., Arling, V. A., Vaughn, B. H., White, J. W. C., and Tans, P. P.: Upward revision of global fossil fuel methane emissions based on isotope database, Nature, 538, 88–91, https://doi.org/10.1038/nature19797, 2016.

Sherwood, O. A., Schwietzke, S., Arling, V. A., and Etiope, G.: Global Inventory of Gas Geochemistry Data from Fossil Fuel, Microbial and Burning Sources, version 2017, Earth System Science Data, 9, 639–656, https://doi.org/10.5194/essd-9-639-2017, 2017.

Tans, P. P.: A note on isotopic ratios and the global atmospheric methane budget, Global Biogeochemical Cycles, 11, 77–81, https://doi.org/10.1029/96GB03940, 1997.

Thanwerdas, J., Saunois, M., Berchet, A., Pison, I., Vaughn, B. H., Michel, S. E., and Bousquet, P.: Variational inverse modeling within the Community Inversion Framework v1.1 to assimilate δ^{13}C(CH_4) and CH_4: a case study with model LMDz-SACS, Geoscientific Model Development, 15, 4831–4851, https://doi.org/10.5194/gmd-15-4831-2022, 2022.

Thompson, R. L., Nisbet, E. G., Pisso, I., Stohl, A., Blake, D., Dlugokencky, E. J., Helmig, D., and White, J. W. C.: Variability in Atmospheric Methane From Fossil Fuel and Microbial Sources Over the Last Three Decades, Geophysical Research Letters, 45, 11,499–11,508, https://doi.org/10.1029/2018GL078127, 2018.

Townsend-Small, A., Tyler, S. C., Pataki, D. E., Xu, X., and Christensen, L. E.: Isotopic measurements of atmospheric methane in Los Angeles, California, USA: Influence of “fugitive” fossil fuel emissions, Journal of Geophysical Research: Atmospheres, 117, https://doi.org/10.1029/2011JD016826, 2012.

Umezawa, T., Brenninkmeijer, C. A. M., Röckmann, T., van der Veen, C., Tyler, S. C., Fujita, R., Morimoto, S., Aoki, S., Sowers, T., Schmitt, J., Bock, M., Beck, J., Fischer, H., Michel, S. E., Vaughn, B. H., Miller, J. B., White, J. W. C., Brailsford, G., Schaefer, H., Sperlich, P., Brand, W. A., Rothe, M., Blunier, T., Lowry, D., Fisher, R. E., Nisbet, E. G., Rice, A. L., Bergamaschi, P., Veidt, C., and Levin, I.: Interlaboratory comparison of δ^{13}C and δD measurements of atmospheric CH_4 for combined use of data sets from different laboratories, Atmospheric Measurement Techniques, 11, 1207–1231, https://doi.org/10.5194/amt-11-1207-2018, 2018.

van der Werf, G. R., Randerson, J. T., Giglio, L., van Leeuwen, T. T., Chen, Y., Rogers, B. M., Mu, M., van Marle, M. J. E., Morton, D. C., Collatz, G. J., Yokelson, R. J., and Kasibhatla, P. S.: Global fire emissions estimates during 1997–2016, Earth System Science Data, 9, 697–720, https://doi.org/10.5194/essd-9-697-2017, 2017.

Voulgarakis, A., Naik, V., Lamarque, J.-F., Shindell, D. T., Young, P. J., Prather, M. J., Wild, O., Field, R. D., Bergmann, D., Cameron-Smith, P., Cionni, I., Collins, W. J., Dalsøren, S. B., Doherty, R. M., Eyring, V., Faluvegi, G., Folberth, G. A., Horowitz, L. W., Josse, B., MacKenzie, I. A., Nagashima, T., Plummer, D. A., Righi, M., Rumbold, S. T., Stevenson, D. S., Strode, S. A., Sudo, K., Szopa, S., and Zeng, G.: Analysis of present day and future OH and methane lifetime in the ACCMIP simulations, Atmospheric Chemistry and Physics, 13, 2563–2587, https://doi.org/10.5194/acp-13-2563-2013, 2013.

Warwick, N. J., Cain, M. L., Fisher, R., France, J. L., Lowry, D., Michel, S. E., Nisbet, E. G., Vaughn, B. H., White, J. W. C., and Pyle, J. A.: Using δ^{13}C-CH_4 and deltaD-CH_4 to constrain Arctic methane emissions, Atmospheric Chemistry and Physics, 16, 14 891–14 908, https://doi.org/10.5194/acp-16-14891-2016, 2016.

Yver, C. E., Pison, I. C., Fortems-Cheiney, A., Schmidt, M., Chevallier, F., Ramonet, M., Jordan, A., Søvde, O. A., Engel, A., Fisher, R. E., Lowry, D., Nisbet, E. G., Levin, I., Hammer, S., Necki, J., Bartyzel, J., Reimann, S., Vollmer, M. K., Steinbacher, M., Aalto, T., Maione, M., Arduini, J., O&apos;Doherty, S., Grant, A., Sturges, W. T., Forster, G. L., Lunder, C. R., Privalov, V., Paramonova, N., Werner, A., and Bousquet, P.: A new estimation of the recent tropospheric molecular hydrogen budget using atmospheric observations and variational inversion, Atmospheric Chemistry and Physics, 11, 3375–3392, https://doi.org/10.5194/acp-11-3375-2011, 2011.

Zazzeri, G., Lowry, D., Fisher, R. E., France, J. L., Lanoisellé, M., Kelly, B. F. J., Necki, J. M., Iverach, C. P., Ginty, E., Zimnoch, M., Jasek, A., and Nisbet, E. G.: Carbon isotopic signature of coal-derived methane emissions to the atmosphere:from coalification to alteration, Atmospheric Chemistry and Physics, 16, 13 669–13 680, https://doi.org/10.5194/acp-16-13669-2016, 2016.

Zhao, Y., Saunois, M., Bousquet, P., Lin, X., Berchet, A., Hegglin, M. I., Canadell, J. G., Jackson, R. B., Hauglustaine, D. A., Szopa, S., Stavert, A. R., Abraham, N. L., Archibald, A. T., Bekki, S., Deushi, M., Jöckel, P., Josse, B., Kinnison, D., Kirner, O., Marécal, V., O’Connor, F. M., Plummer, D. A., Revell, L. E., Rozanov, E., Stenke, A., Strode, S., Tilmes, S., Dlugokencky, E. J., and Zheng, B.: Inter-model comparison of global hydroxyl radical (OH) distributions and their impact on atmospheric methane over the 2000–2016 period, Atmospheric Chemistry and Physics, 19, 13 701–13 723, https://doi.org/10.5194/acp-19-13701-2019, 2019.